NATIONAL ENERGY TECHNOLOGY LABORATORY

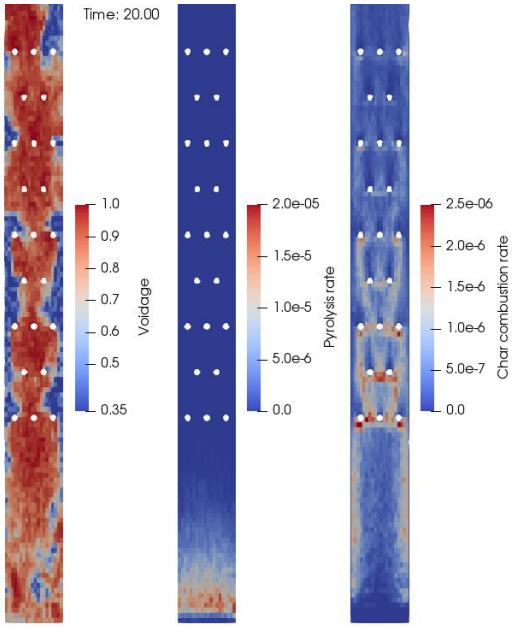

Biomass Combustion in a Circulating Fluidized Bed Combustor

10 September 2020

U.S. DEPARTMENT OF ENERGY | NATIONAL ENERGY TECHNOLOGY LABORATORY

Office of Fossil Energy

DOE/NETL-2020/2148

Disclaimer

This work was funded by the Department of Energy, National Energy Technology Laboratory, an agency of the United States Government, through a support contract with Leidos Research Support Team (LRST).

Cover Illustration: Detail of the combustion zone in the lower riser.

Suggested Citation: Banerjee, S.; Hughes, R. *Biomass Combustion in a Circulating Fluidized Bed Combustor*; DOE.NETL-2020.2148; NETL Technical Report Series; U.S. Department of Energy, National Energy Technology Laboratory: Morgantown, WV, 2020; p 32. DOE: 10.2172/1659115.

Biomass Combustion in a Circulating Fluidized Bed Combustor

Subhodeep Banerjee[1,2], Robin W. Hughes[3]

[1] U.S. Department of Energy, National Energy Technology Laboratory, Leidos Research Support Team, 3610 Collins Ferry Road, Morgantown, WV 26507

[2] U.S. Department of Energy, National Energy Technology Laboratory, Oak Ridge Institute for Science and Education, 3610 Collins Ferry Road, Morgantown, WV 26507

[3] Natural Resources Canada, CanmetENERGY, 1 Haanel Drive, Ottawa, ON, Canada

---

DOE/NETL-2020/2148

10 September 2020

NETL Contacts:

William A. Rogers, Principal Investigator

Jonathan Lekse, Technical Portfolio Lead

Bryan Morreale, Executive Director, Research & Innovation Center

This page intentionally left blank.

Table of Contents

List of Figures

List of Tables

Acronyms, Abbreviations, and Symbols

Term	Description
BECCS	Bio-energy CCS
CCS	Carbon capture and storage
CFB	Circulating fluidized bed
CFD	Computational fluid dynamics
DOE	U.S. Department of Energy
MFiX	Multiphase Flow with interphase eXchanges
NETL	National Energy Technology Laboratory
NRCan	Natural Resources Canada
PIC	Particle-in-cell

Acknowledgments

This work was performed in support of the U.S. Department of Energy's (DOE) Fossil Energy Crosscutting Technology Research Program. The research was executed through the National Energy Technology Laboratory's (NETL) Research and Innovation Center's Advanced Reaction Systems Field Work Proposal. The research was supported in part by an appointment to the U.S. DOE's Postgraduate Research Program at NETL administered by the Oak Ridge Institute for Science and Education. Research performed by Leidos Research Support Team staff was conducted under the RSS contract 89243318CFE000003.

The author acknowledges the help provided by the NETL Multiphase Flow Science group, specifically the consultations with and contributions from Jeff Dietiker, Mehrdad Shahnam, Xi Gao, Deepthi Chandramouli, and William Rogers.

The author and NETL acknowledge Robin Hughes and his experimental team and Allan Runstedtler at Natural Resources Canada, CanmetENERGY, for their support of this collaboration, for sharing valuable data from their 50kW$_{th}$ test facility, and for their extensive consultation on problem set up and data interpretation.

EXECUTIVE SUMMARY

Interest in circulating fluidized bed (CFB) boilers as a power generation technology has sky-rocketed in recent years because of several advantages this technology offers over conventional boilers, such as increased gas-solid mixing resulting in higher combustion efficiency and the ability to use lower quality fuels. CFB combustors are operated at lower temperatures than conventional thermal power generation combustors, thus reducing NO_x emissions. SO_2 emissions are conveniently controlled through the addition of Ca-based sulphur sorbents within the combustor.

This report summarizes the current modeling effort on a 50 kW_{th} CFB combustor with a diameter of 10 cm and a height of 5 m; designed, built, and operated at CanmetENERGY in Ottawa, Canada employing the multiphase particle-in-cell (PIC) approach in the open-source Multiphase Flow with Interphase eXchanges (MFiX) Software Suite. The MFiX-PIC model parameters for the simulation are tuned against cold-flow experiments from CanmetENERGY using 9 kg of olivine sand as the inert bed material. It is shown that for the relatively coarse fluid meshes and large parcel sizes necessitated by the scale of the simulation, filter size dependent corrections to the drag law must be incorporated to ensure accuracy of the simulation results.

The validated cold flow model is extended to simulate reacting flow with torrefied hardwood as the feedstock and to validate the combustion reaction scheme. The species concentrations at the riser outlet are compared against CanmetENERGY's experiments and show satisfactory agreement. The simulations demonstrate the ability of MFiX-PIC to accurately capture the physics and chemistry of a circulating fluidized bed combustor at bench scales, which can be further extended to pilot- and industrial-scale systems.

1. INTRODUCTION

The circulating fluidized bed (CFB) boiler is a relatively new power generation technology that offers several advantages over conventional boilers. The high superficial gas velocity in a CFB combustor leads to increased gas-solid mixing resulting in higher efficiency and the fuel can circulate until fully burned. CFB combustors utilize a flameless combustion process operated at lower temperatures than conventional thermal power generation units, thus reducing the production of NO_x. SO_2 emissions can be conveniently controlled through the addition of Ca-based sulfur sorbents within the combustor (Basu and Fraser, 1991). The presence of the hot sands comprising the bed in a CFB combustor allow even lower grade fuels such as lignites, coal wastes, biomass, and other industrial and agricultural waste to be combusted with high efficiency (Anthony, 1995; Koornneef et al., 2007). The largest CFB combustors in use today are 460–600 MW_e (Leckner et al., 2016).

Initial development of computational fluid dynamics (CFD) models of CFB combustors focused on small-scale systems (Basu, 1999; Gungor and Eskin, 20008; Adamczyk et al., 2014). More recently, the 340 MWe boiler operated by Korea South-East Power Corporation was modeled by Farid et al. (2017) achieving 600 s of simulation over 5 months. A comprehensive CFD model of a CFB boiler must include hydrodynamics, wall heat transfer model, and combustion models (Xu et al., 2019). The bulk of the development in numerical models for CFB combustion at large scales have been limited to hydrodynamics only (Zhang et al., 2010; Jiang et al. 2014; Shi et al., 2014; Xie et al., 2018) or focused on oxy-fuel combustion (Duan et al., 2014; Tan et al., 2014; Xu et al., 2015; Liu et al., 2019); only a few authors reported comprehensive numerical models for biomass CFB combustors (Varol et al., 2014; Morin et al., 2018).

Biomass can be considered a carbon-neutral energy source since it uptakes CO_2 from the atmosphere as it grows and releases it back to the atmosphere when it is burned. Over the last decade, bioenergy increased from 8% of the world's total primary energy supply to 10%, and it has been projected to rise further to 25–33% by 2050 (EIA, 2013). The U.S. generates 93 million tons of biomass waste annually, but power generation using biomass is still in its nascence (The Independent, 2016). When biomass is used in a carbon capture and storage (CCS) system the CO_2 can be removed from the atmosphere and subsequently stored in geological formations—this is referred to as bio-energy CCS (BECCS). BECCS is considered a negative emission technology that provides an intelligent approach to reducing the concentration of greenhouse gases in the atmosphere (Rogeli et al., 2018). Oxyfuel combustion is one of the leading CO_2 capture technologies that is being studied extensively for BECCS.

This work represents a collaborative effort between CanmetENERGY, a division of Natural Resources Canada (NRCan) and the U.S. Department of Energy (DOE) National Energy Technology Laboratory (NETL) in the study of CFB combustion of coal and biomass over a range of oxyfuel conditions. NRCan has been doing extensive experiments with their 50 kW_{th} CFB combustion system which allows for a range of coal-biomass mixtures under air and oxyfuel conditions. In this work, a CFD model of their 50 kW_{th} biomass combustor is developed to understand and analyze the complex gas-solid hydrodynamics, chemical processes, and energy conversion in the bench-scale system, and the scale-up considerations required to develop the industrial-scale CFB combustors of the future.

2. NUMERICAL SOLUTION APPROACH

The modeling work in this report is performed using the multiphase particle-in-cell (PIC) module in the open-source code Multiphase Flow with Interphase eXchanges (MFiX). In this methodology, first proposed by Andrews and O'Rourke (1996) and extended to three-dimensional systems by Snider (2001), the gas is modeled as an Eulerian continuum phase and the solids are grouped into discrete parcels containing particles with similar properties that are tracked individually.

The Navier-Stokes equations for fluid motion are slightly modified to account for the presence of solid particles done by including the porosity, which is defined equal to the volume fraction of the fluid, ϵ_f in the computational cell on which the equations are applied. Source terms are added to account for the transfer of mass, momentum, and energy between solid and gas phases. The volume-averaged continuity equation, momentum equations, and energy equation can be written as:

$$\frac{\partial}{\partial t}\left(\epsilon_f \rho_f\right) + \nabla \cdot \left(\epsilon_f \rho_f \boldsymbol{u}_f\right) = \dot{m}_{sg} \tag{1}$$

$$\frac{\partial}{\partial t}\left(\epsilon_f \rho_f \boldsymbol{u}_f\right) + \nabla \cdot \left(\epsilon_f \rho_f \boldsymbol{u}_f \boldsymbol{u}_f\right) = -\epsilon_f \nabla p_f - \nabla \cdot \bar{\bar{\tau}}_f + \epsilon_f \rho_f \mathbf{g} - \boldsymbol{K}_{sg} \tag{2}$$

$$\frac{\partial}{\partial t}\left(\epsilon_f \rho_f E\right) + \nabla \cdot \left(\epsilon_f \boldsymbol{u}_f \left(\rho_f E + p_f\right)\right) = \nabla \cdot \left(k \nabla T - \sum h_j \boldsymbol{J}_j + \left(\bar{\bar{\tau}}_f \cdot \boldsymbol{u}_f\right)\right) + S_h \tag{3}$$

where ρ_f, $\boldsymbol{u}_f$, p_f, E, and T are the density, velocity, pressure, internal energy, and temperature of the fluid respectively; $\mathbf{g}$ is the acceleration due to gravity; k is the conductivity; and h_j and $\boldsymbol{J}_j$ are the enthalpy and diffusion flux of species j. The source term in the momentum equation, $\boldsymbol{K}_{sg}$ is used to couple the solid and gas phases by accounting for the solid-gas momentum exchange from the inter-phase drag due to the presence of the solid particles. The source terms in the continuity and energy equations, $\dot{m}_{sg}$ and S_h, capture the mass and heat fluxes from the solid to the gas phase due to chemical reactions in the multiphase flow. For a Newtonian fluid, the shear stress tensor, τ_f can be written as:

$$\bar{\bar{\tau}}_f = \mu_f \left(\nabla \boldsymbol{u}_f + \nabla \boldsymbol{u}_f^T\right) - \frac{2}{3}\mu_f \nabla \boldsymbol{u}_f \bar{\bar{I}} \tag{4}$$

where μ_f is the fluid viscosity.

The position and velocity of the parcels of solid particles is resolved by Newton's second law of motion.

$$\frac{d\boldsymbol{x}_p}{dt} = \boldsymbol{u}_p \tag{5}$$

$$\frac{d\boldsymbol{u}_p}{dt} = -\frac{\nabla p}{\rho_p} + \mathbf{F}_{contact} + \mathbf{F}_{drag} + \mathbf{g} \tag{6}$$

The drag force, $\mathbf{F}_{drag}$ in Equation (6) accounts for the transfer of momentum from the fluid to a solid particle as it moves through each cell, and is modeled as:

$$\boldsymbol{F}_{drag} = F_D\left(\boldsymbol{u}_f - \boldsymbol{u}_p\right) \tag{7}$$

where $\boldsymbol{u}_f$ is the fluid velocity, $\boldsymbol{u}_p$ is the particle velocity, and F_D is the net drag coefficient. The net drag coefficient can be obtained from:

$$F_D = \frac{18\mu_f}{\rho_p d_p^2}\frac{C_D Re_p}{24} \tag{8}$$

where μ_f, ρ_p, and d_p are the viscosity of the fluid and the density and diameter of the solid particle respectively. C_D and Re_p are the particle drag coefficient for a sphere and the relative Reynolds number based on the particle diameter.

$$Re_p = \frac{\rho_f d_p|\boldsymbol{u}_f - \boldsymbol{u}_p|}{\mu_f} \tag{9}$$

The corresponding momentum transfer from the solid phase to the gas phase is incorporated by adding the source term $\boldsymbol{K}_{sg} = \beta_{sg}\left(\boldsymbol{u}_f - \boldsymbol{u}_p\right)$ in the momentum equation for the gas phase.

Several numerical models exist for the drag coefficient in the literature. The drag model of Gidaspow (1992) is initially used in this study. Among the homogeneous drag models, it is a good candidate for fluidized bed simulations that include a range of solid loadings because it accounts for the differences in solid-gas interaction in the dilute and densely packed regions by switching between the drag prediction of the Ergun equation (1952) and the drag model of Wen and Yu (1966) based on the solids volume fraction. For $\epsilon_s > 0.8$, the Gidaspow drag model gives:

$$\beta_{sg} = \frac{3}{4}C_D\frac{\epsilon_s\epsilon_g\rho_g|\boldsymbol{u}_f - \boldsymbol{u}_p|}{d_p}\epsilon_g^{-2.65}; C_D = \frac{24}{\epsilon_g \mathrm{Re}_p}\left[1 + 0.15\left(\alpha_g \mathrm{Re}_p\right)^{0.687}\right] \tag{10}$$

Conversely, for $\epsilon_s \leq 0.8$,

$$\beta_{sg} = 150\frac{\epsilon_s\left(1-\epsilon_g\right)\mu_g}{\epsilon_g d_p^2} + 1.75\frac{\rho_g\epsilon_s|\boldsymbol{u}_f - \boldsymbol{u}_p|}{d_p} \tag{11}$$

It has been long established that mesoscale structures such as bubbles and clusters can coexist in turbulent fluidized beds (Bi et al., 2000; Zhu et al., 2008). Obtaining an accurate prediction of the drag requires accurate modeling of these mesoscale effects. The homogeneous drag models such as Gidaspow (1992) can correctly predict the fluidization behavior when the grid size is 2–4 times the particle diameter for bubbling fluidized beds (Wang et al., 2009; Hong et al., 2016) or 10 times for circulating fluidized beds (Agrawal et al., 2001; Benyahia et al. 2007; Igci et al., 2008; Li et al., 2014), but their performance starts to degrade when coarse-graining the model by combining individual particles into parcels. A comparative study of eight drag models, three homogeneous and five homogenous, demonstrated the need to modify the homogeneous models to account for the mesoscale structures to achieve accurate drag prediction in coarse grid simulations (Gao et al., 2018). The authors proposed an enhanced version of the filtered drag model based on Sarkar et al. (2016) that produced superior predictions across all fluidization regimes.

For the bench-scale simulations conducted in this study, the cell size is reasonable compared to the parcel sizes, but each individual particle diameter is approximately one-eighth the parcel diameter and falls below the recommended grid resolution for a circulating fluidized bed to achieve accurate results with the homogeneous drag models. The enhanced filtered drag model of Gao et al. (2018) is thus employed to correctly account for the effect of mesoscale structures on the drag.

The contact force, $\mathbf{F}_{contact}$ in Equation (6) accounts for the inter-particle interactions. In the PIC method, the particle collisions are not resolved directly, and the contact force is expressed as the gradient of the solids stress tensor (DOE, 2020) as given by:

$$\mathbf{F}_{contact} = \frac{\nabla \bar{\bar{\tau}}_s}{\epsilon_s \rho_p} \tag{12}$$

where:

$$\bar{\bar{\tau}}_s = \frac{P_p \epsilon_s^{\gamma}}{\max\left[\left(\epsilon_{cp} - \epsilon_s\right), \delta(1 - \epsilon_s)\right]} \tag{13}$$

In Equation (13), ϵ_{cp} is the void fraction at close packing, which is set to 0.34 based on the packing limit and δ is set at a low value of 10^{-7} to avoid a singularity near the packing limit. The choice for the independent parameters P_p, the linear scale factor, and γ, the exponential scale factor, are not well-established in the literature and have to be determined on a case-by-case basis.

3. EXPERIMENT AND MODELING SETUP

The experimental basis for the simulations in this work is a 50 kW_{th} CFB combustor designed, built, and operated at CanmetENERGY, Natural Resources Canada (Hughes et al., 2015). Geometry specifications and experimental conditions and results were shared directly by email, including experiments conducted for model validation. The goal of the modeling effort was to develop a bench-scale model of a CFB combustor and to validate the model with experimental data for use in further studies over a range of conditions.

A description of the combustor is provided in Hughes et al. (2015) and Sun et al. (2017). The system consists of a stainless-steel riser with an internal diameter of 10 cm and a height of 5 m. The riser is outfitted with electric heaters capable of reaching temperatures up to 1050°C that were used during the preheating stage and for controlling the temperature along the entire length of the riser. The combustor is fed with biomass via a pressurized feed hopper and conveying line through the bottom of the bed. A heat exchanger tube assembly in the bed is used to control the bed temperature by flowing cooling air through the tubes. A schematic of the combustor is shown in Figure 1.

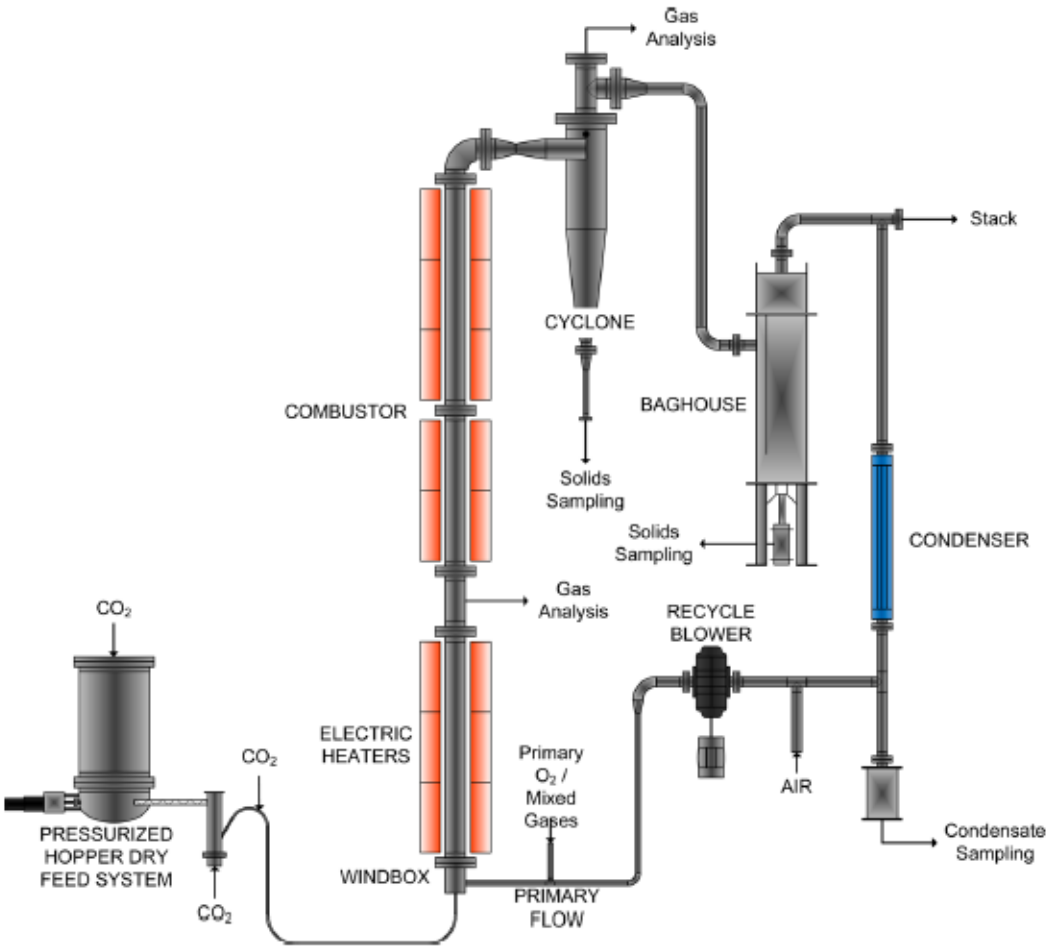

Figure 1: Schematic of the 50 kW_{th} combustor at NRCan (Hughes et al., 2015).

Only the riser is modeled in the current work. The schematic of the CFB riser at NRCan is shown in Figure 2(a,b) and the simplified geometry used in the simulation is shown in Figure 2(c). A Cartesian grid discretizes the computational domain into 0.005 m × 0.008 m × 0.005 m cells and the cut-cell approach is used to truncate the boundary cells to conform to the domain surface (DOE, 2020).

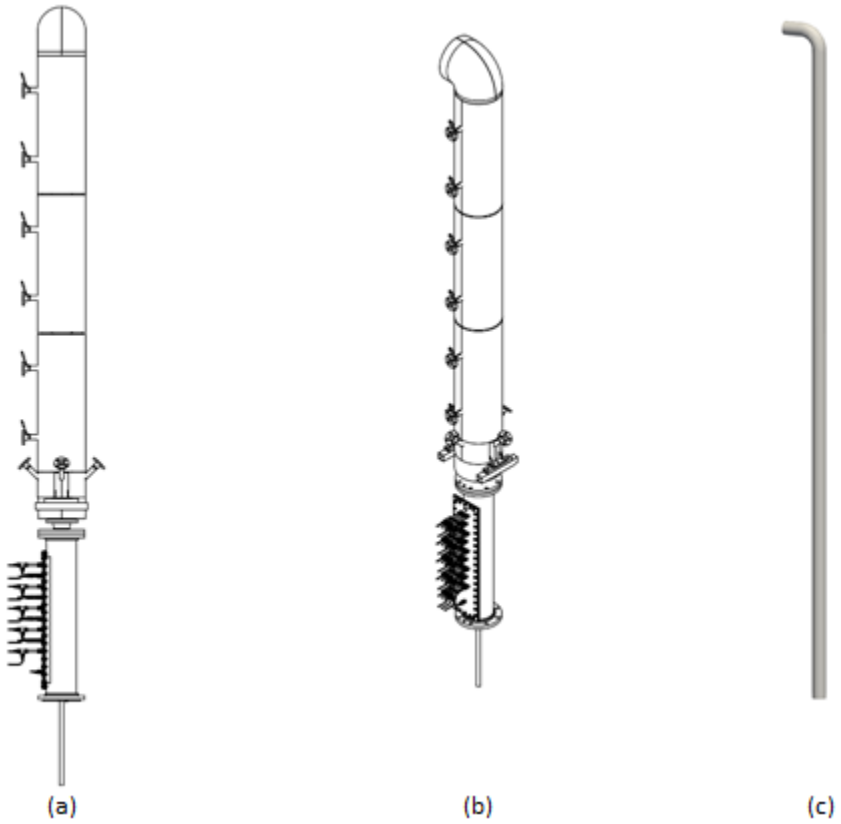

Figure 2: Schematic of the 50 kW_{th} CFBC riser and simplified geometry for simulation (Hughes, 2019).

The biomass feedstock used in the combustion experiments is torrefied hardwood with a particle size distribution as shown in Figure 3. In the simulation, individual biomass parcels are grouped into parcels with a statistical weight of 100. The particle diameter is set at 375 μm, corresponding to d_{50} from Figure 3, equal to 375 μm, and the particle density is 520 kg/m³.

The inert material used in the experiments is roughly 40 wt.% fine olivine sand (150–310 μm) and 60 wt.% coarse olivine sand (310–411 μm) with a density of 3,063 kg/m³. The size distribution of sand is implemented in the simulation by distributing it across seven bins, each with a statistical weight of 500.

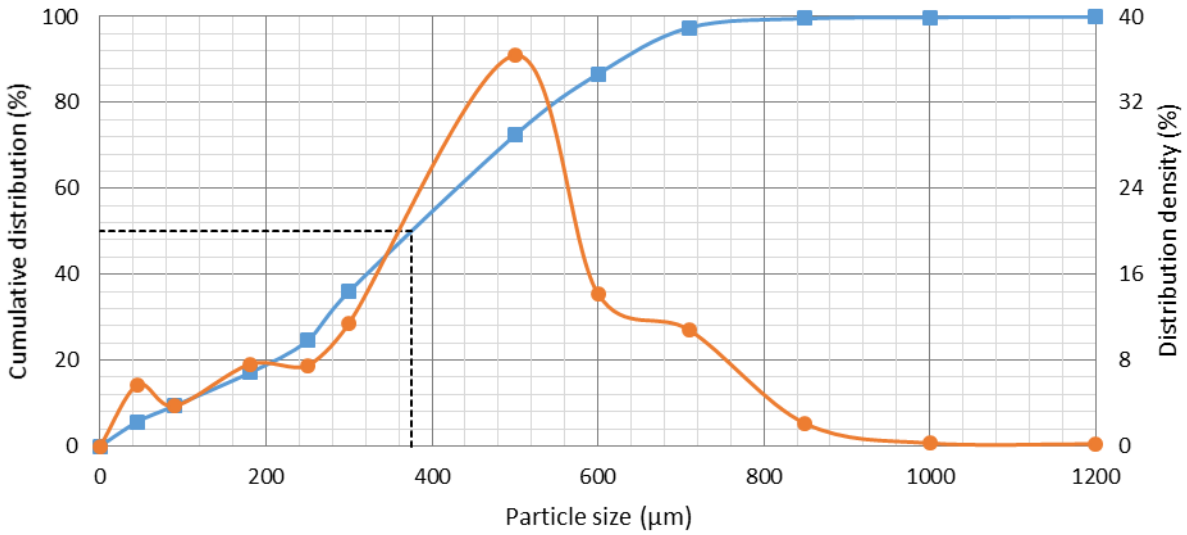

Figure 3: Particle size distribution of the torrefied hardwood feedstock.

The bottom of the riser is set as a mass inlet with a mass flow rate of 18.06 kg/h of air modeled as 80 vol.% N_2 and 20 vol.% O_2) and 2.65 kg/h of biomass. The walls of the riser are set at 850°C in line with the experiment; the walls of the heat exchanger tubes are also set at 850°C. The effect of cooling air flow through heat exchanger tubes to maintain the bed temperature in the NRCan riser will be implemented in the future by prescribing the heat flux across the tube surfaces. The riser outflow is modeled as a pressure outlet and the gas composition is continuously monitored.

4. HYDRODYNAMICS BENCHMARKING

The fluidization behavior in the absence of combustion was assessed in a series of experiments conducted at NRCan. An inert bed consisting of 9.0 kg olivine sand was fluidized by air with varying fluidization velocities U_g and no biomass feed. The temperature of the fluidizing air was set at 120ºC to better match the pressure drop obtained during the combustion experiments. The pressure drop in the lower and upper regions in the riser are reported in Table 1; the results of the combustion experiment at 850ºC are also shown.

Table 1: Test Cases for Inert Simulations Compared against Combustion Pressure Drop (Hughes, 2019)

	Non-Circulating			Circulating		Combustion
U_g (m/s)	0.40	0.70	1.56	3.09	5.94	-
T_{avg} (°C)	120.8	120.0	124.0	122.7	115.2	850.0
ΔP_1 (kPa)	7.8	7.8	6.8	3.9	0.1	4.3
ΔP_2 (kPa)	0.0	0.0	0.0	0.8	1.2	0.5

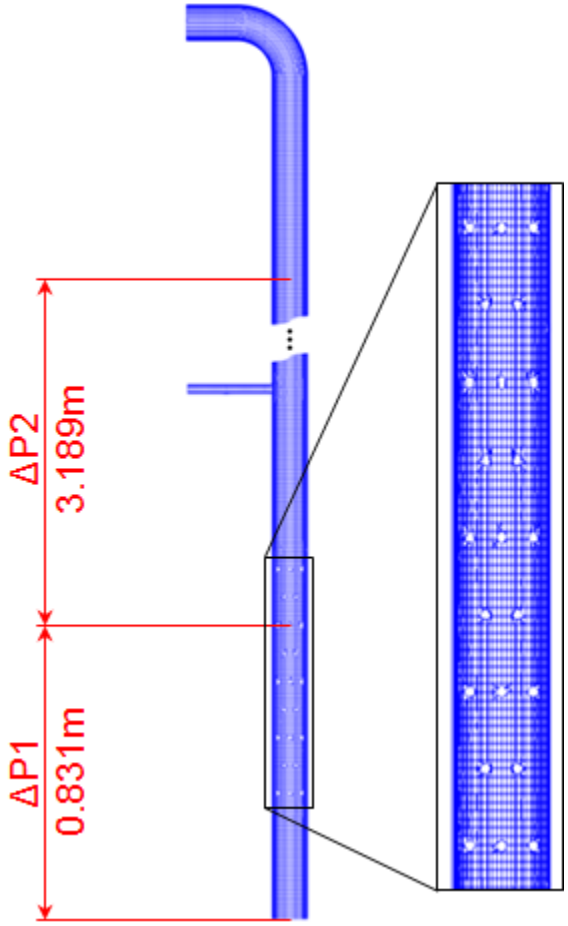

Figure 4: Computational grid for riser only simulations with details of tube bank.

At low fluidization velocities up to and including 1.56 m/s, the bed is in the bubbling fluidization regime with no circulation, as evidenced by the zero to low pressure drop in the upper riser. Of the inert runs, the case with U_g = 3.09 m/s has the pressure drops closest to that in the combustion experiment at 850ºC. Hence, this is the case selected to investigate the effect of the scaling parameters P_p and γ in Equation (13) for the present application.

Preliminary simulations showed that the fluidization behavior in the riser is insensitive to γ but has a strong dependence on P_p. Therefore, γ is left unchanged from its default value of 3.0 and a parametric study is conducted to establish the optimum value of P_p. In order to complete multiple simulations as required for the parametric study in a shorter timeframe, the complexity of the geometry is reduced by modeling only the riser, as shown in Figure 4. As the sand particles are elutriated out of the riser, they must be recirculated back into the riser to maintain the solids inventory. To achieve this, a recirculation algorithm is implemented into MFiX whereby the sand particles are allowed to leave the reactor until a prescribed recirculating inventory is reached. For U_g = 3.09 m/s, the recirculating inventory is specified at half the initial loading, equal to 4.5 kg, based on input from NRCan. Once the solids inventory reaches this value, any additional particles that leave the system are reinjected with a constant axial velocity via the side inlet shown in Figure 4 to maintain the total inventory at the prescribed value.

The recirculation algorithm can be seen in action in Figure 5, which shows the time evolution of pressure drop and inventory in the riser for P_p = 5. The overall inventory in the system drops from 9.0 kg to 4.5 kg in about 14 s as sand particles are elutriated at which point the recirculation flag is triggered. From this point onwards, all particles leaving the system are reinjected back so the total inventory remains constant at 4.5 kg.

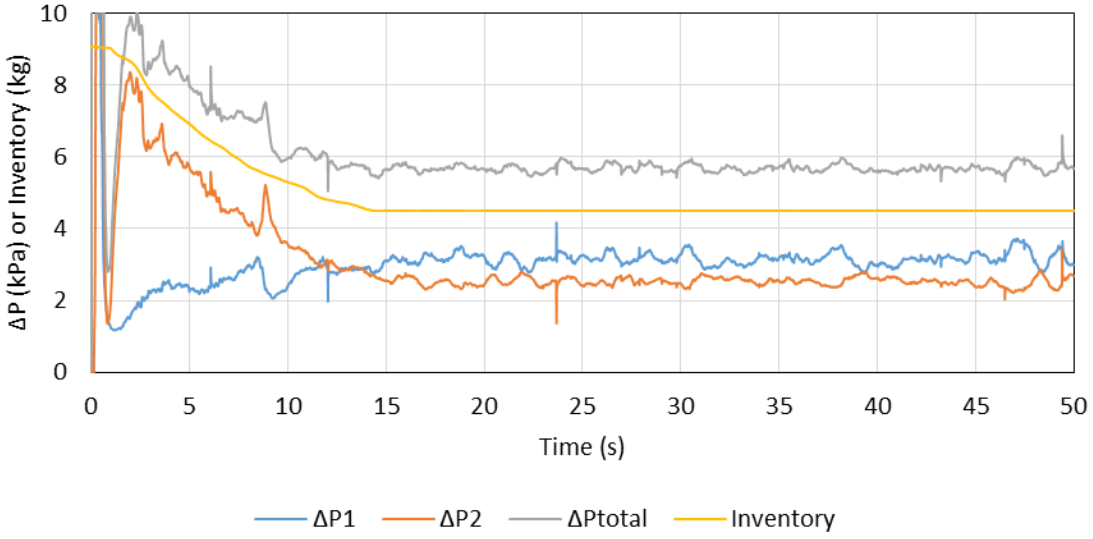

Figure 5: Time evolution of pressure drop and inventory for U_g = 3.09 m/s with P_p = 5, γ = 3.

The inert simulation is conducted for a range of values of P_p equal to 1, 5, 10, and 100 (default) with the Gidaspow drag law (1992). The time-averaged pressure drop in the lower and upper sections for each run is obtained from the final 10 s of simulation and compared in Figure 6 and

shows almost identical results. The plot of the particle size distribution of the recirculating inventory shown in Figure 7 is more instructive. Recalling Equation (13), the solids stress increases linearly with P_p holding γ constant, which aggravates solid motion. At P_p = 5, the solids stress is smaller and the finer, lighter particles are significantly more fluidized compared to the coarser, heavier particles. By the time the initial inventory drops to 4.5 kg, only 20% of the smallest particles remain in the riser compared to nearly 95% of the largest. On the other hand, for P_p = 100, the final recirculating inventory comprises 40% of the smallest particles and 80% of the heaviest. The effect of P_p on the pressure drop distribution is canceled out by its effect on the particle size distribution.

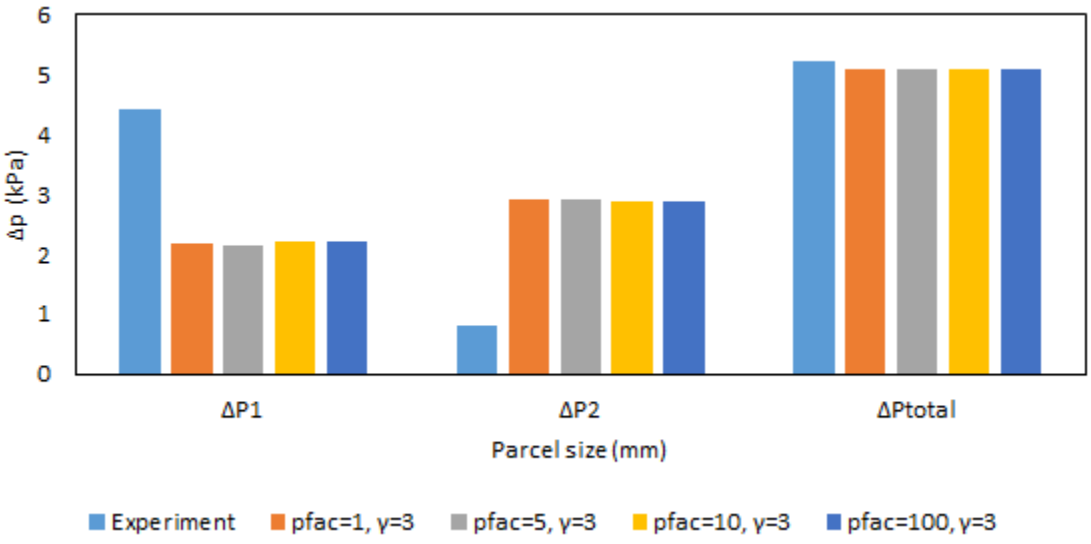

Figure 6: Effect of P_p on the time-average pressure drop.

For all values of P_p, the total pressure drop shown in Figure 6 matches the experimental value exactly. This is expected as the total pressure drop is a measure of the total recirculating inventory, which was prescribed based on the experimental value. However, the pressure drop distribution between the lower and upper sections of the riser show a large discrepancy and indicates significant over-fluidization compared to the experiment. Reducing the tangential restitution coefficient, η_{tw} from the default value of 1.0 to 0.85 to increase energy losses from particle collisions with the riser walls and the heat exchanger tubes is considered to reduce the over-fluidization behavior; the results are shown in Figure 8 for P_p = 1, γ = 3. Reducing the restitution coefficient did serve to de-fluidize the upper riser, but the effect was minimal. Even reducing the restitution coefficient to an extreme 0.1 could not match the experimental behavior.

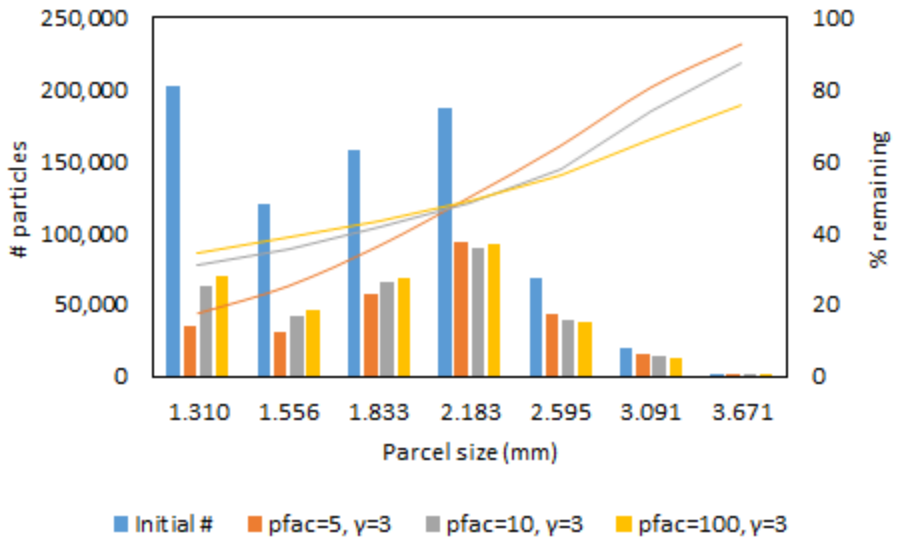

Figure 7: Effect of P_p on the particle size distribution of the recirculating inventory.

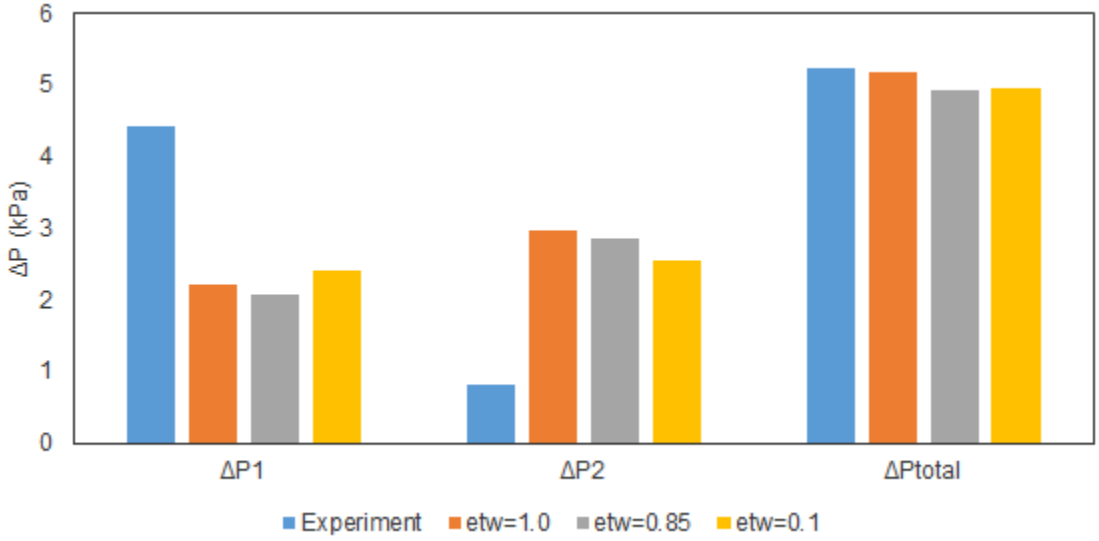

Figure 8: Effect of the tangential restitution coefficient on the time-averaged pressure drop.

Next, the enhanced filtered drag model is investigated as a means to reduce the over-fluidization with a more accurate drag prediction by taking into account the effect of mesoscale structures (Gao et al., 2018). The time evolution of inventory and pressure drop using the filtered drag model are compared against the Gidaspow results in Figure 9 using $P_p = 1$, $\gamma = 3$. Using the Gidaspow drag model, the initial inventory drops to the prescribed recirculating inventory of 4.5 kg in about 21 s; for the filtered drag model, this time increases to over 150 s. After the initial "slug" of solids are elutriated, the bulk of the remaining solids remain in the lower riser and the solids flux out of the reactor slows to a trickle, indicating that the over-fluidization behavior has been mitigated. The time evolution of the pressure drops also shows that while the total pressure

drop using the filtered drag model approaches that using the Gidaspow model around 120 s, the pressure drop in the lower riser is significantly higher than that in the upper riser. The time-averaged pressure drops shown in Figure 10 affirms that the filtered drag model successfully addresses the issue of over-fluidization in the riser and the predicted pressure drop distribution matches the experimental results.

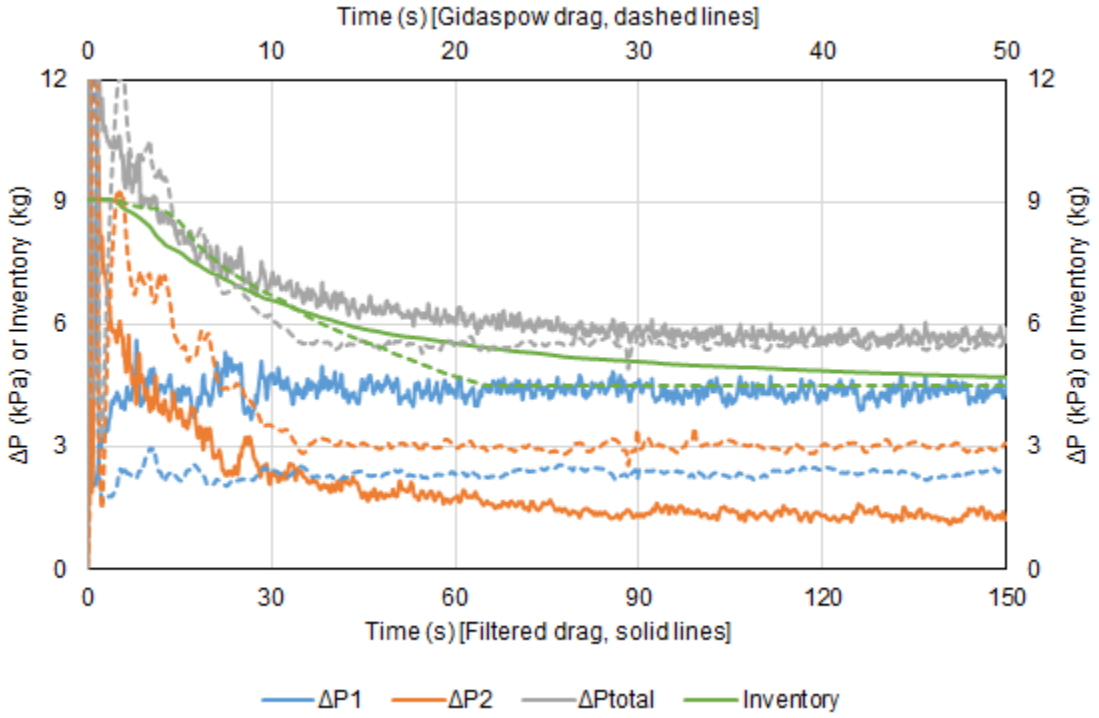

Figure 9: Comparison of time evolution of pressure drop and inventory using different drag closures.

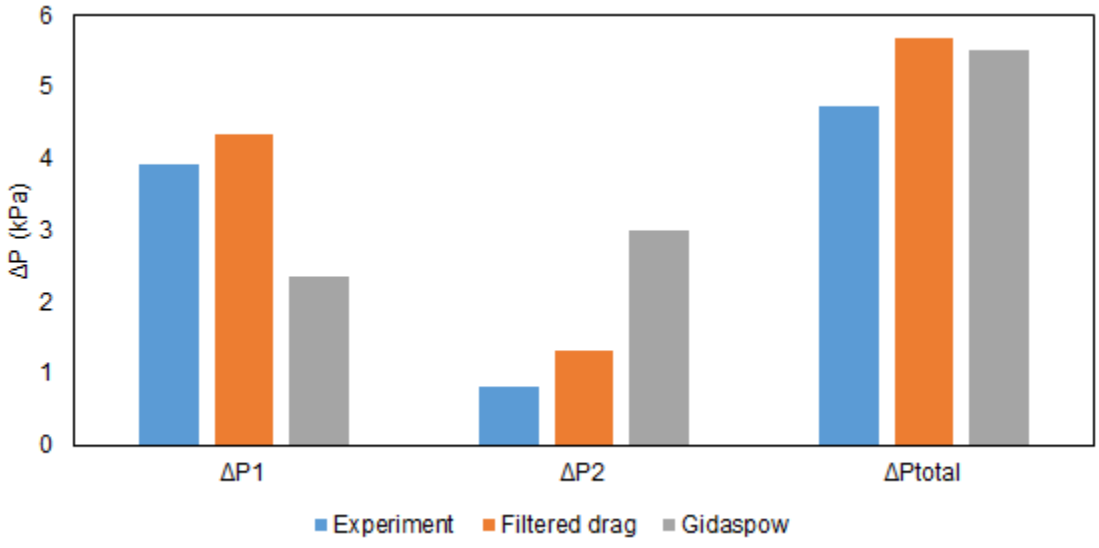

Figure 10: Comparison of the time-averaged pressure drop using different drag closures.

4.1 CHEMICAL REACTION MODELING

With a robust model in place for capturing the hydrodynamics of the NRCan CFB combustor, the chemical reaction mechanisms to model the biomass combustion process can be incorporated. The reaction scheme used in this work is outlined in Table 2 and the corresponding rate kinetics are provided in Table 3.

Table 2: Combustion Reaction Scheme

#	Description	Reaction
1	Pyrolysis	$Volatiles_{(s)} \rightarrow 0.2281 \cdot CO + 0.1657 \cdot CO_2 + 0.1493 \cdot H_2 + 0.1012 \cdot CH_4 + 0.2399 \cdot Char_{(s)} + 0.1158 \cdot Tar$
2	Char combustion	$Char_{(s)} + O_2 \rightarrow CO_2$
3	Water gas shift reaction	$CO + H_2O \leftrightarrow CO_2 + H_2$
4	Carbon monoxide combustion	$CO + 0.5 \cdot O_2 \rightarrow CO_2$
5	Methane combustion	$CH_4 + 2 \cdot O2 \rightarrow CO_2 + 2\ H_2O$
6	Hydrogen combustion	$H_2 + 0.5 \cdot O_2 \rightarrow H_2O$

Note: The tar produced by pyrolysis is left untreated in the current work while different tar combustion schemes are investigated.

Table 3: Chemical Kinetics for Combustion Scheme

#	Description (Source)	Reaction Rate
1	Pyrolysis (see note)	$r_{pyrolysis} = 2 \times 10^{19} \mathrm{e}^{\frac{-212180}{8.314 T_b}} \frac{m_b}{MW_b}$
2	Char combustion (Field et al., 1967)	$r_{char} = \frac{p_{O_2} S_{char}}{MW_{O_2}\left[\frac{1}{k_{film}} + \frac{1}{k_{reaction}}\right]}$
3	Water gas shift reaction (Biba et al., 1978)	$r_{WGS} = 2.78 \cdot 10^6 \mathrm{e}^{\frac{-1515}{T_g}} \left(1 - 1/0.0265 \mathrm{e}^{\frac{-3958}{T_g}}\right) c_{CO} c_{H_2O}$
4	Carbon monoxide combustion (Westbrook and Dryer, 1981)	$r_{CO} = 1.30 \cdot 10^{14} \mathrm{e}^{\frac{-15098}{T_g}} c_{O_2}^{0.5} c_{CO} c_{H_2O}^{0.5}$
5	Methane combustion (Westbrook and Dryer, 1981)	$r_{CH_4} = 6.70 \cdot 10^{11} \mathrm{e}^{\frac{-24360}{T_g}} c_{O_2}^{1.3} c_{CH_4}^{0.2}$
6	Hydrogen combustion (Peters, 1979)	$r_{H_2} = 1.08 \cdot 10^{16} \mathrm{e}^{\frac{-15098}{T_g}} c_{O_2} c_{H_2}$

Note: The pyrolysis rate is based on the kinetics scheme developed at NETL for cypress, a low-ash hardwood similar to the feedstock used in the NRCan experiments based on proximate analysis.

The initial results from the combustion simulations are obtained using a monodisperse sand bed with particle diameter equal to 331 μm based on d_{50}. Figure 11 shows the time evolution of total biomass inventory in the riser. The biomass inventory increases in the first 20 s of simulation, but reaches a pseudosteady state thereafter. It is noted that the biomass inventory is approximately 4 orders of magnitude smaller than the circulating sand inventory so its effect on the pressure drop is likely to be negligible. The biomass feed rates and the chemical reaction scheme, once validated, can be incorporated into the polydisperse sand bed used in the inert simulations without loss of hydrodynamic fidelity.

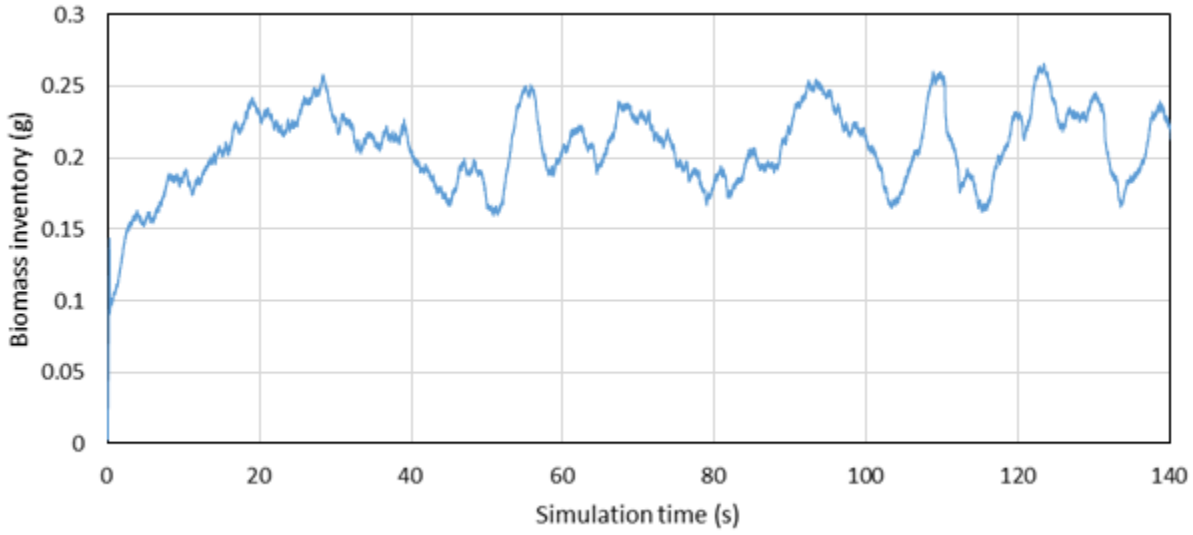

Figure 11: Time evolution of total biomass inventory in riser.

The size evolution of the biomass as a result of the pyrolysis and char combustion reactions in the first one second of simulation is shown in Figure 12. Each particle in the figure represents a parcel of biomass enlarged 20x for visualization. The fresh (dry) biomass enters at room temperature with 76.86 wt.% volatiles, 21.98 wt.% char, and 1.16 wt.% ash. At the operating temperature of 850°C, pyrolysis occurs near instantaneously in the vicinity of the biomass injection port and leads to a reduction in size of the biomass particles. This is followed by oxidation of the char remaining in the biomass as the particles move up the riser. By the time the particles reach the outlet, the char is completely converted and the particles leaving the reactor are primarily ash as shown in Figure 12.

The outlet species concentrations of CO_2 and O_2 for experimental and model predictions are shown in Figure 13; the predicted trace gases are shown in Figure 14. The predicted concentrations of CO_2 and O_2 are in excellent agreement with the experiment. Most of the trace gas species at the outlet reach a steady state within 5 s of simulation time except H_2. The time evolution of H_2 reflects the initial accumulation of biomass in the reactor. Once the biomass inventory starts to level off, the rate of depletion of H_2 as a result of oxidation offsets the rate of production of H_2 by pyrolysis and a steady-state value is reached. The only trace gas with a reported concentration is CO at 20 ppm; this discrepancy may be due to incomplete combustion

of tar in the experiment producing additional CO. A tar combustion scheme needs to be added to the model in the future to mitigate this.

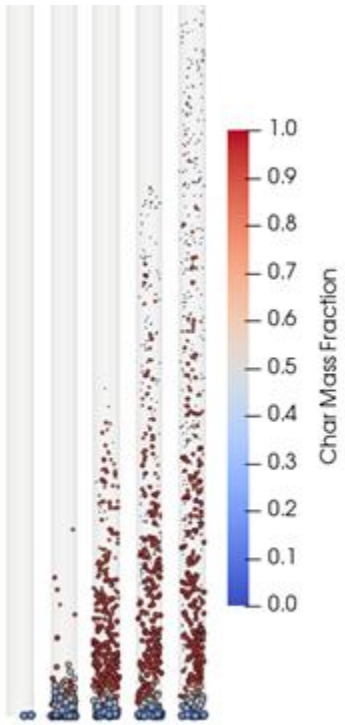

Figure 12: Size evolution of biomass particles as a result of pyrolysis and char combustion.

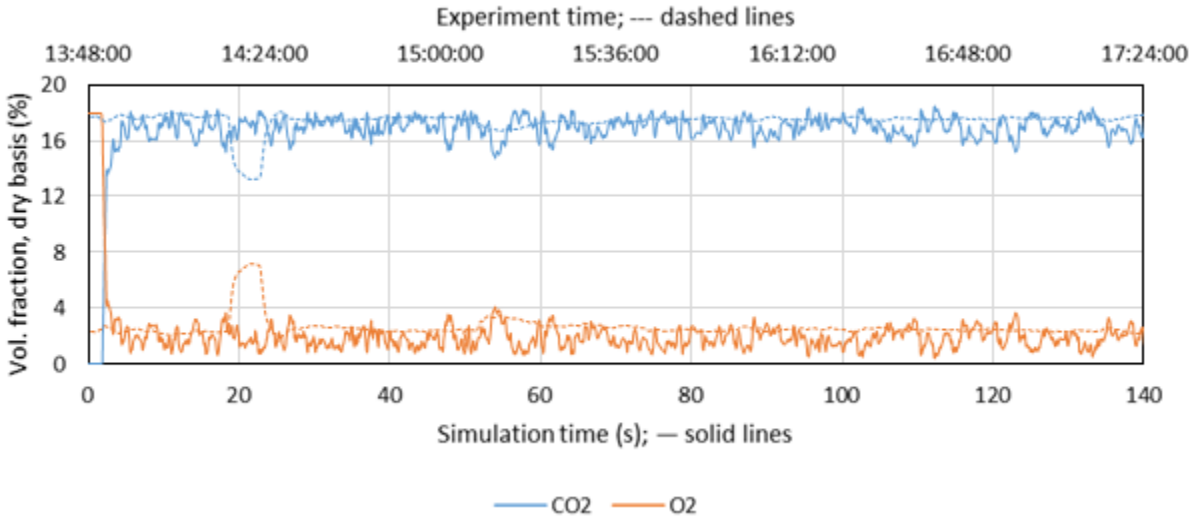

Figure 13: Time evolution of the concentration of CO_2 and O_2 at the riser outlet.

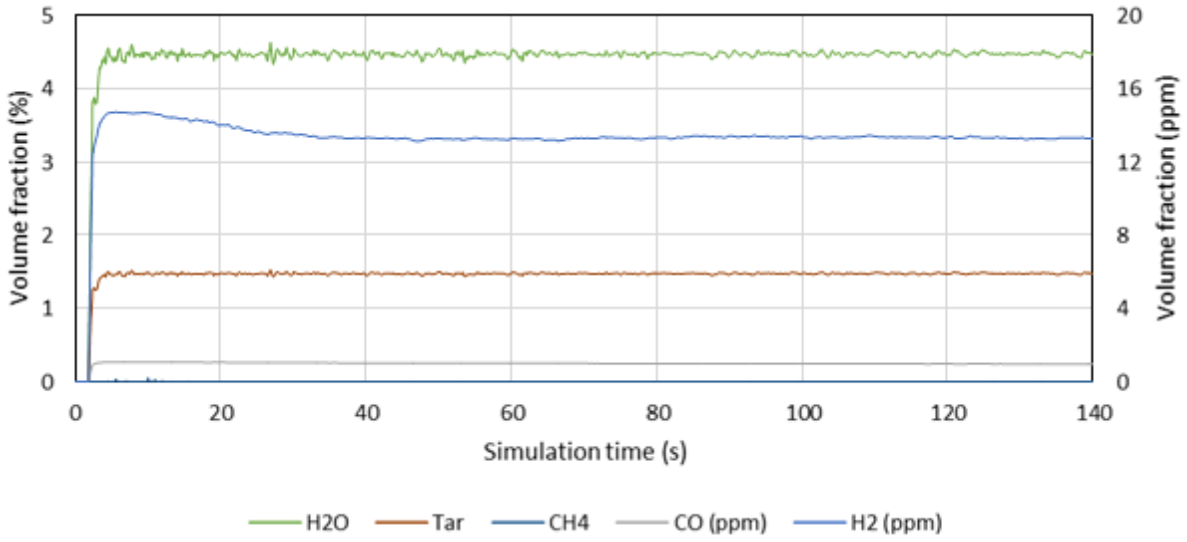

Figure 14: Time evolution of the concentration of trace gases at the riser outlet.

The initial results from the combustion simulation show excellent agreement with the experiment in terms of the gas concentrations and validate the combustion reaction scheme incorporated in the model. Next, the simulations are conducted with the polydisperse sand bed to better integrate the reaction scheme with the actual hydrodynamics of the system. The species concentrations of CO_2 and O_2 at the outlet are shown in Figure 15. Compared to the results in Figure 13 for the simulation with the monodisperse sand bed, no significant differences are observed, which suggests that the hydrodynamics of the sand phase has limited impact on the fluidization and combustion of the biomass particles. This is a shortcoming of the PIC approach since it does not consider inter-particle collisions.

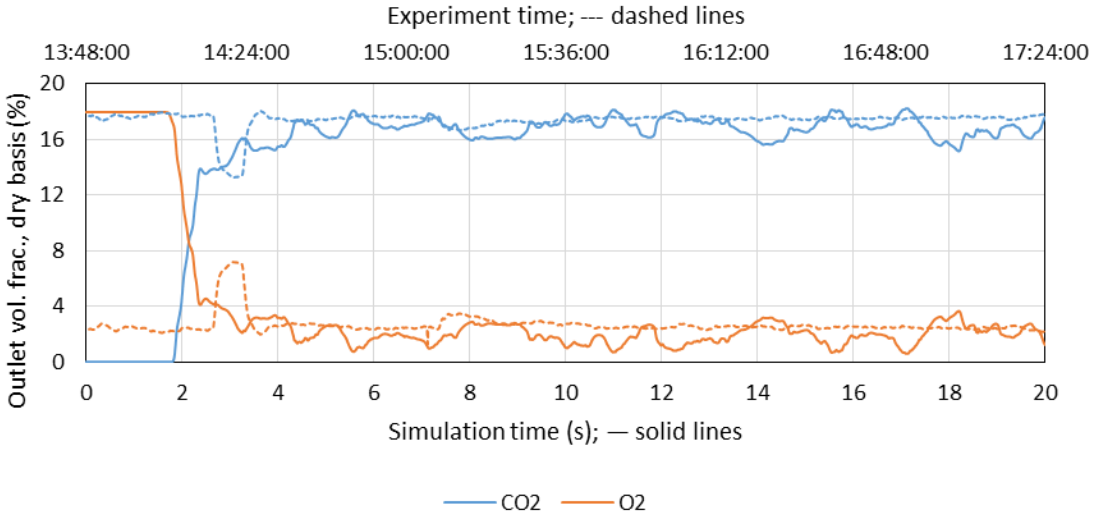

Figure 15: Time evolution of the concentration of CO_2 and O_2 at the riser outlet (polydisperse sand bed).

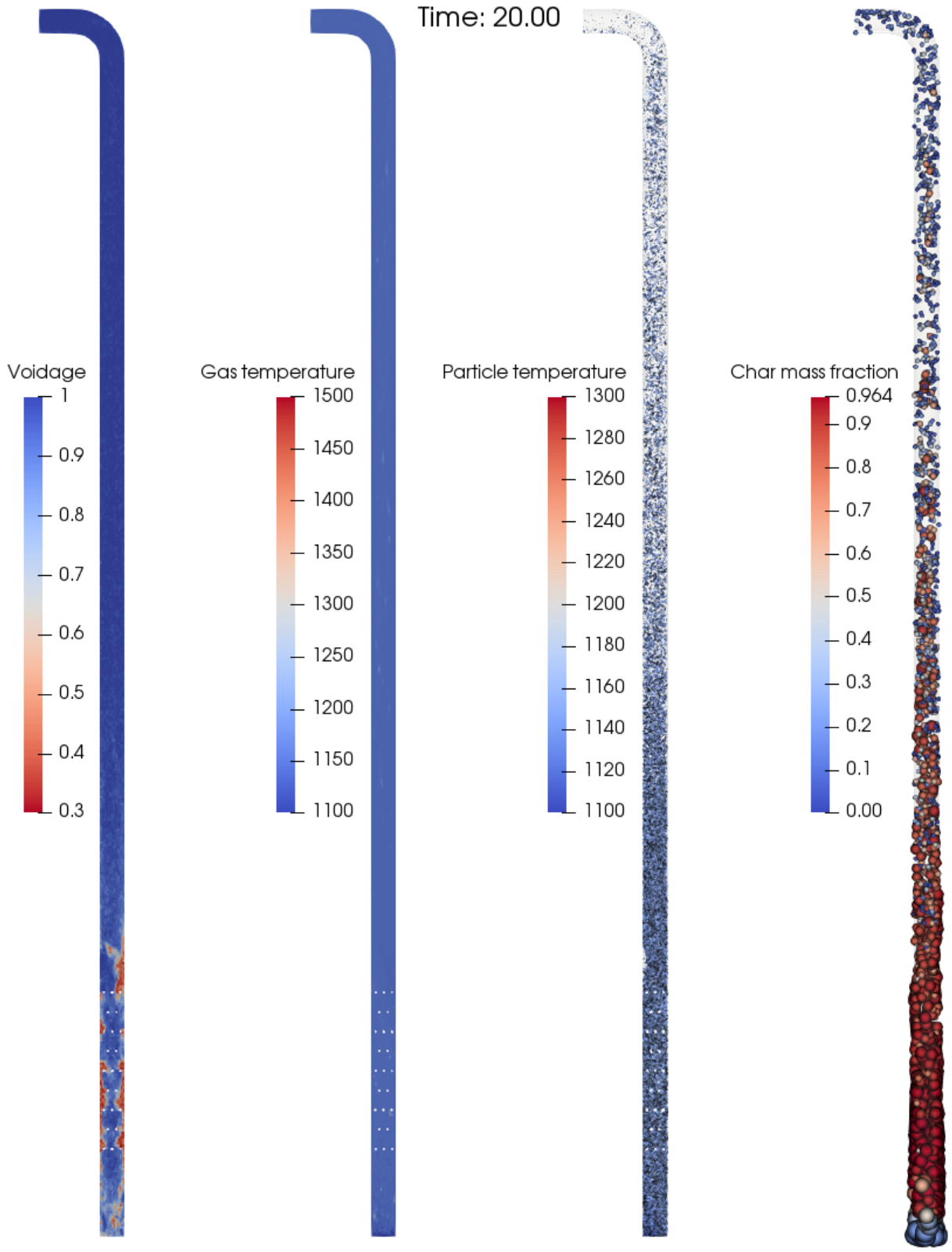

Figure 16: Snapshot of riser after 20 s of simulation.

Figure 16 shows a snapshot of the voidage, gas temperature, particle temperature, and char mass fraction in the riser after 20 s of simulation. The lowest voidage, corresponding to the highest density of sand particles, occurs near the walls, which may further explain the weak interaction between the sand and biomass phases. The gas and particle temperatures (in Kelvin) after 20 s are distributed roughly uniformly, in line with the experimental results. This is verified by plotting the temperature profile in Figure 17. The size evolution of the biomass particles is reflected in the char mass fractions. From the snapshot, it can be observed that the largest decrease in biomass particle size, corresponding to the highest rate of char combustion, is in the lower riser, and the char is completely converted by the time the particles reach the riser outlet.

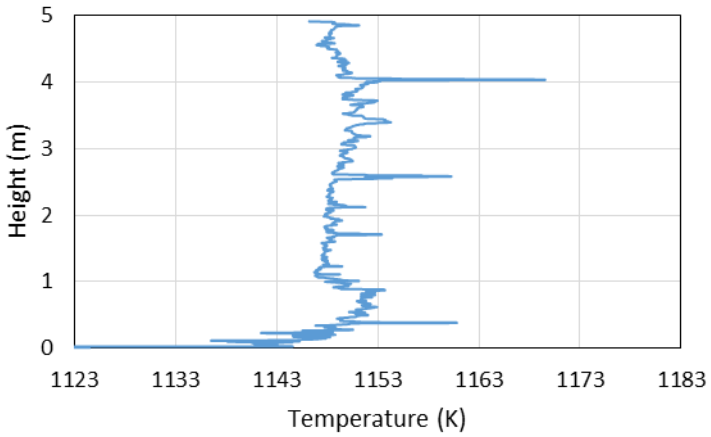

Figure 17: Temperature profile along riser centerline after 20 s of simulation.

A detailed snapshot of the voidage as well as the pyrolysis and char combustion reaction rates in the lower riser after 20 s are shown in Figure 18. The pyrolysis and combustion zones can be identified from Figure 18. The pyrolysis reaction occurs to completion adjacent to the biomass inlet. The highest char combustion rates occur in the stagnation and wake zones of the heat exchanger tubes, which suggests that they also serve a secondary purpose of breaking up the gas bubbles and bypass pathways and increasing the local residence time of the biomass particles.

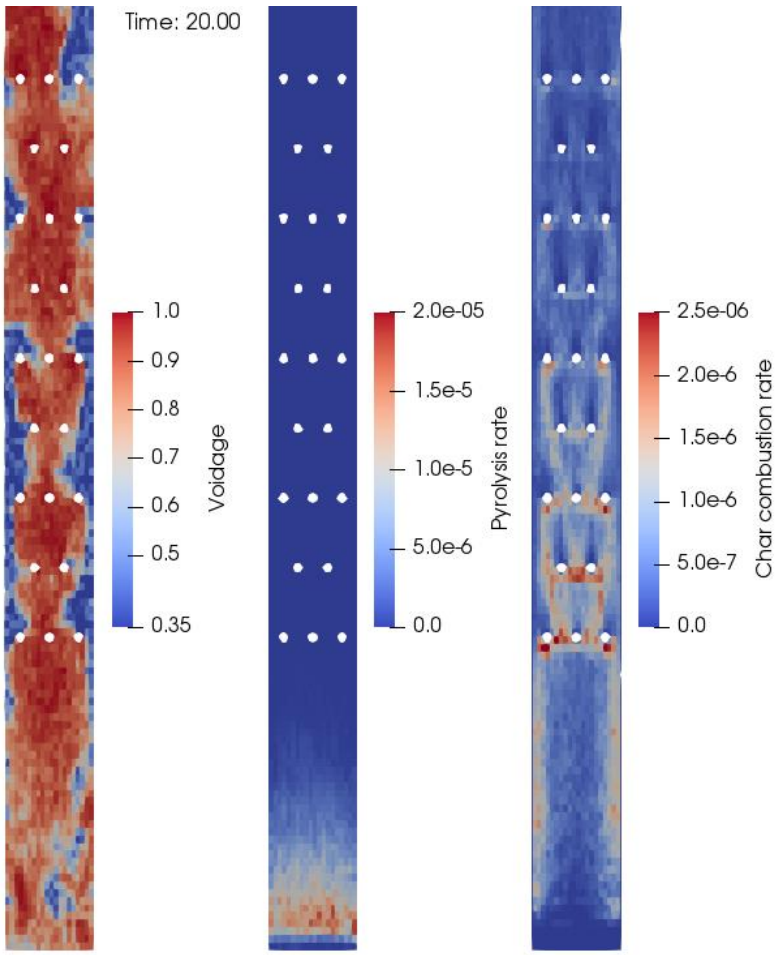

Figure 18: Detailed snapshot of the lower riser after 20 s of simulation.

5. CONCLUSIONS AND FUTURE WORK

This report summarizes the current status in the collaborative work modeling the 50 kW_{th} CFB combustor designed, built, and operated at CanmetENERGY, a division of Natural Resources Canada in Ottawa, Canada (Hughes et al., 2015) employing the multiphase PIC approach in the open-source MFiX Software Suite.

The hydrodynamics of the riser are validated against experiment via inert simulations using 9.0 kg of olivine sand as the bed material. A parametric study is conducted on the linear scale factor in the solids stress model in MFiX-PIC to obtain the optimum value to match the pressure drop distribution in the experimental riser. Furthermore, it is shown that for the relatively coarse fluid grid and large parcel sizes necessitated by the scale of the simulation, filter-size dependent corrections to the homogeneous drag laws must be incorporated to take into account the mesoscale effects such as bubbles and clusters to ensure accuracy of the simulation results.

The validated cold-flow model is extended to simulate reacting flow with torrefied hardwood as the feedstock and validate the combustion reaction scheme. The species concentrations at the riser outlet are compared against NRCan's experiment and show satisfactory agreement. The simulations demonstrate the ability of MFiX-PIC to accurately capture the physics and chemistry of a circulating fluidized bed combustor at bench scales, which can be further extended to pilot- and industrial-scale systems.

During the hydrodynamics validation, it was observed that by forcing the prescribed riser inventory at all times, the recirculation algorithm artificially dampened the pressure fluctuations in the riser. To mitigate these issues, it is desirable in the future to model the full loop, including the cyclone and standpipe, so that the particle recirculation can be allowed to evolve on its own without the need to prescribe the riser inventory. The variance in the circulation rates as a function of the flow conditions would also provide additional data points to validate the model.

Figure 19 shows a model of the full-loop geometry that is the subject of ongoing work as well as the results of an inert simulation after 20 s. The particle tracks in Figure 19 show the sand particles being separated in the cyclone and conveyed back to the riser through the standpipe. However, the void fraction in the standpipe is nearly one instead of being close to the packing limit as expected. As a result, the riser inventory stays around 8.5 kg instead of 4.5 kg. This suggests that some form of flow control mechanism such as a loop-seal is required in the standpipe to maintain the particle residence time in the standpipe. This is currently being investigated under consultation with NRCan.

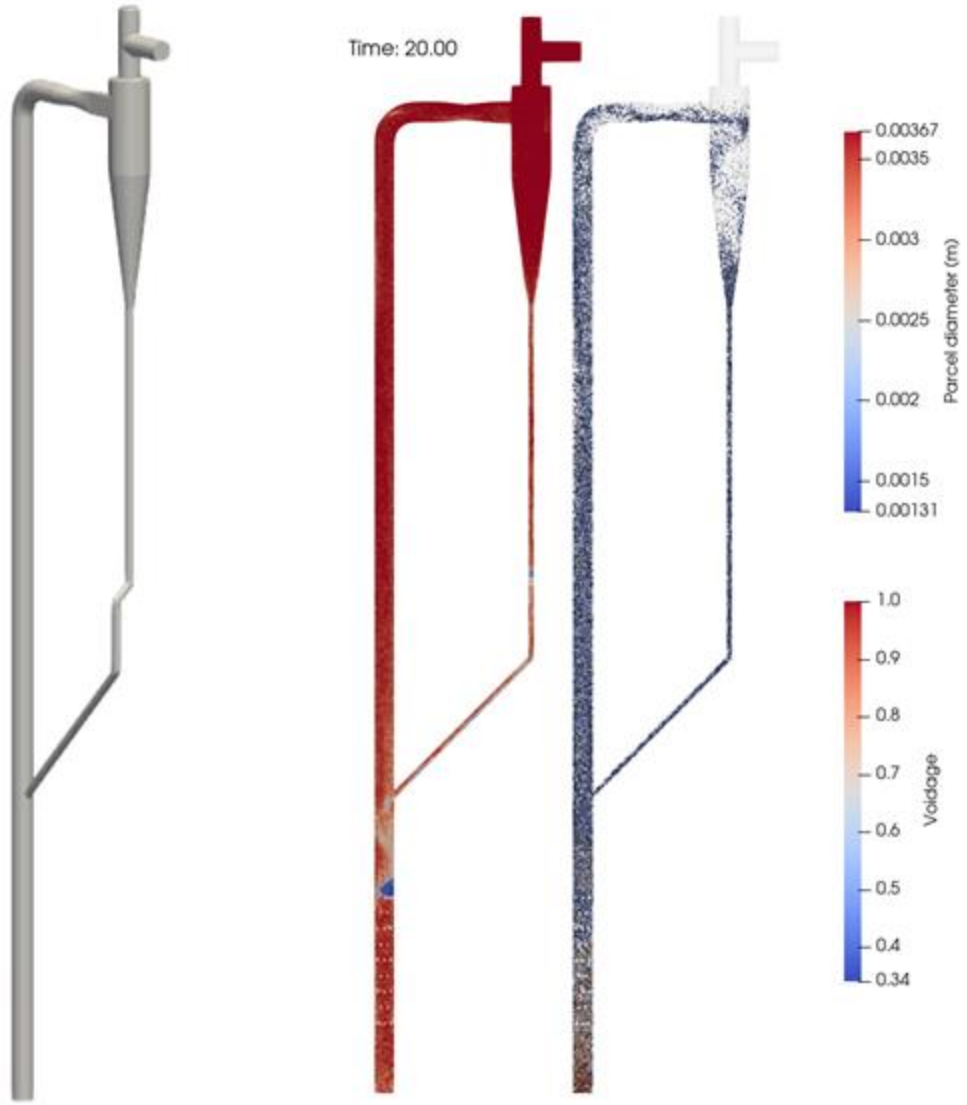

Figure 19: Full-loop geometry of the NRCan CFB combustor and snapshot of preliminary simulation.

Additionally, it was observed from the chemical reaction modeling that since the combustor is operated using excess oxygen, the pyrolysis products CO, CH_4, and H_2 are completely consumed or remain only in trace amounts at the ppm level. A simplified combustion mechanism is currently under investigation whereby the pyrolysis vapor is modeled as a single pseudospecies, followed by a one reaction combustion step to produce CO_2 and H_2O. Since the gas-phase combustion reactions tend to be stiff, reducing the number of gas-phase reactions in the combustion scheme may lead to significant time savings. Finally, the effect of cooling air flow through heat exchanger tubes to maintain the bed temperature in the NRCan riser needs to be implemented by prescribing the heat flux across the tube surfaces in the simulation.

6. REFERENCES

Adamczyk, W. P.; Wecel, G.; Klajny, M.; Kozolub, P.; Klimanek, A.; Bialecki, R. Modeling of particle transport and combustion phenomena in a large-scale circulating fluidized bed boiler using a hybrid Euler–Lagrange approach. *Particuology* **2014,** *16*, 29–40.

Agrawal, K.; Loezos, P. N.; Syamlal, M.; Sundaresan, S. The role of meso-scale structures in rapid gas–solid flows. *J. Fluid Mech.* **2001,** *445*, 151–85.

Andrews, M. J.; O'Rourke, P. J. The multiphase particle-in-cell (MP-PIC) method for dense particle flow. *Int. J. Multiphase Flow* **1996,** *22*, 379–402.

Anthony, E. J. Fluidized bed combustion of alternative solid fuels; status, successes and problems of the technology. *Prog. Energy Comb. Sci.* **1995,** *21*, 239–68.

Basu, P. Combustion of coal in circulating fluidized-bed boilers: A review. *Chem. Eng. Sci.* **1999,** *54*, 5547–57.

Basu, P.; Fraser, S. A. *Circulating Fluidized Bed Boilers: Design and Operations*, 1st ed.; Butterworth-Heinemann: Waltham, MA, 1991.

Benyahia, S.; Syamlal, M.; O'Brien, T. J. Study of the ability of multiphase continuum models to predict core-annulus flow. *AIChE J.* **2007,** *53*, 2549–68.

Biba, V.; Macak, J.; Klose, E.; Malecha, J. Mathematical model for the gasification of coal under pressure. *Ind. Eng. Chem. Process. Des. Dev.* **1978,** *17*, 92–98.

Bi, H. T.; Ellis, N.; Abba, I. A.; Grace, J. R. A state-of-the-art review of gas–solid turbulent fluidization. *Chem. Eng. Sci.* **2000,** *55*, 4789–825.

Duan, L.; Sun, H.; Zhao, C.; Zhou, W. Coal combustion characteristics on an oxy-fuel circulating fluidized bed combustor with warm flue gas recycle. *Fuel* **2014,** *127*, 47–51.

EIA. Energy Information Administration, International Energy Outlook 2013. U.S. Department of Energy: Washington, DC, 2013.

Ergun, S. Fluid flow through packed columns. *Chem. Eng. Prog.* **1952,** *48*, 89–94.

Farid, M. M.; Jeong, H. J.; Kim, K. H.; Lee, J. Numerical investigation of particle transport hydrodynamics and coal combustion in an industrial-scale circulating fluidized bed combustor: Effects of coal feeder positions and coal feeding rates. *Fuel* **2017,** *192*, 187–200.

Field, M.; Gill, D.; Morgan, B.; Hawksley, P. *Combustion of Pulverized Coal*; British Coal Utilisation Research Association (BCURA): Leatherhead, UK, 1967.

Gao, X.; Tingwen, L.; Avik, S.; Lu, L.; Rogers, W. A. Development and validation of an enhanced filtered drag model for simulating gas-solid fluidization of Geldart A particles in all flow regimes. *Chem. Eng. Sci.* **2018,** *184*, 33–51.

Gidaspow, D. *Multiphase Flow and Fluidization*; Academic Press: San Diego, CA, 1992.

Gungor, A.; Eskin, N. Two-dimensional coal combustion modeling of CFB. *Int. J. Thermal Sci.* 2008, 47, 157–74.

Hong, K.; Chen, S.; Wang, W.; Li, J. Fine-grid two-fluid modeling of fluidization of Geldart A particles. *Powder Technol.* **2016,** *296*, 2–16.

Hughes, R.W., et al. Oxy-fluidized bed combustion using under bed fines fuel injection. In 22nd International Conference on Fluidized Bed Conversion, Turku, Finland, 2015.

Igci, Y.; Andrews, A. T.; Sundaresan, S.; Pannala, S. Filtered two-fluid models for fluidized gas-particle suspensions. *AIChE J.* **2008,** *54*, 1431–48.

Jiang, Y.; Qiu, G.; Wang, H. Modelling and experimental investigation of the full-loop gas–solid flow in a circulating fluidized bed with six cyclone separators. *Chem. Eng. Sci.* **2014,** *109*, 85–97.

Koornneef, J.; Junginger, M.; Faaij, A. Development of fluidized bed combustion—An overview of trends, performance and cost. *Prog. Energy Comb. Sci.* **2007,** 19–55.

Leckner, B.; Thorson, L.; Kjärstad, J.; Johnsson, F. Utilization of fluidized bed boilers—a worldwide overview. In 73rd IEA-FBC Technical Meeting. Tokyo, Japan, 2016.

Li, T.; Gel, A.; Pannala, S.; Shahnam, M. CFD simulations of circulating fluidized bed risers. Part I: Grid study. *Powder Technol.* **2014,** *254*, 170–180.

Liu, D.; Li, W.; Li, S.; Song, W.; Liu, D. Kong, R. Transformation characteristics of sodium, chlorine and sulfur of Zhundong coal during O_2/CO_2 combustion in circulating fluidized bed. *Energy* **2019,** *185*, 254–61.

DOE. The MFiX 19.3 User Guide, Release 19.3.0. MFS Development Group, Department of Energy: Morgantown, WV, 2020.

Morin, M.; Pécate, S.; Hémati, M. Kinetic study of biomass char combustion in a low temperature fluidized bed. *Chem. Eng. J.* **2018,** *331*, 265–77.

Peters, N. Premixed burning in diffusion flames—the flame zone model of Libby and Economos. *Int. J. Heat and Mass Transfer* **1979,** *22*, 691–703.

Rogelj, J.; Shindell, D.; Jiang, K. Mitigation Pathways Compatible with 1.5°C in the Context of Sustainable Development. In *Global Warming of 1.5°C. An IPCC Special Report*, 2018.

Sarkar, A.; Milioli, F. E.; Ozarkar, S.; Li, T. Filtered sub-grid constitutive models for fluidized gas-particle flows constructed from 3-D simulations. *Chem. Eng. Sci.* **2016,** *152*, 443–56.

Shi, X.; Lan, X.; Liu, F.; Zhang, Y.; Gao, J. Effect of particle size distribution on hydrodynamics and solids back-mixing in CFB risers using CPFD simulation. *Powder Technol.* **2014,** *266*, 135–43.

Snider, D.M. An incompressible three-dimensional multiphase particle-in-cell model for dense particle flows. *J. Comp. Phys.* **2001,** *170*, 523–49.

Sun, Z.; Lu, D. Y.; Ridha, F. N.; Hughes, R. W. Enhanced performance of ilmenite modified by CeO_2, ZrO_2, NiO, and Mn_2O_3 as oxygen carriers in chemical looping combustion. *Applied Energy* **2017,** *195*, 303–15.

Tan, L.; Li, S.; Li, W.; Shou, E. Effects of oxygen staging and excess oxygen on O_2CO_2 combustion with a high oxygen concentration in a circulating fluidized bed. *Energy Fuels* **2014,** *28*, 2069–75.

The Independent. Green energy: How one power plant chips away at the UK's carbon footprint. 2016. https://www.independent.co.uk/environment/green-energy-how-one-power-plant-chips-away-at-the-uks-carbon-footprint-a6796716.html (accessed 26 March 2020).

Varol, M.; Atimtay, A.T.; Olgun, H.; Atakül, H. Emission characteristics of co-combustion of a low calorie and high sulfur–lignite coal and woodchips in a circulating fluidized bed combustor: Part 1. Effect of excess air ratio. *Fuel* **2014,** *117*, 792–800.

Wang, J.; van der Hoef, M.; Kuipers, J. A. M. Why the two-fluid model fails to predict the bed expansion characteristics of Geldart A particles in gas-fluidized beds: a tentative answer. *Chem. Eng. Sci.* **2009,** 64, 622–25.

Wen, C. Y.; Yu, H. Y. Mechanics of fluidization. *Chem. Eng. Prog. Symp. Ser.* **1966,** *62*, 100–11.

Westbook, C. K.; Dryer, F. L. Simplified reaction mechanisms for the oxidation of hydrocarbon fuels in flames. *Comb. Sci. Technol.* **1981,** *27*, 31–43.

Xie, J.; Zhong, W.; Yu, A. MP-PIC modeling of CFB risers with homogeneous and heterogeneous drag models. *Adv. Powder Technol.* **2018,** *29*, 2859–71.

Xu, L.; Cheng, L.; Ji, J.; Wang, Q. A comprehensive CFD combustion model for supercritical CFB boilers. *Particuology* **2019,** *43*, 29–37.

Xu, M.; Li, S.; Li, W.; Lu, Q. Effects of gas staging on the NO emission during O_2/CO_2 combustion with high oxygen concentration in circulating fluidized bed. *Energy Fuels* **2015,** *29*, 3302–11.

Zhang, N.; Lu, B.; Wang, W.; Li, J. 3D CFD simulation of hydrodynamics of a 150MWe circulating fluidized bed boiler. *Chem. Eng. J.* **2010,** *162*, 821–28.

Zhu, H.; Zhu, J.; Li, G.; Li, F. Detailed measurements of flow structure inside a dense gas–solids fluidized bed. *Powder Technol.* **2008,** *180*, 339–49.

This page intentionally left blank.

Brian Anderson, Ph.D.
Director
National Energy Technology Laboratory
U.S. Department of Energy

John Wimer
Associate Director
Strategic Planning
Science & Technology Strategic Plans & Programs
National Energy Technology Laboratory
U.S. Department of Energy

Bryan Morreale
Executive Director
Research & Innovation Center
National Energy Technology Laboratory
U.S. Department of Energy